JOURNAL OF THERMOPHYSICS AND HEAT TRANSFER
Vol. 10, No. 2, April–June 1996

Numerical Simulation of Nonequilibrium Condensation in a Hypersonic Wind Tunnel

E. R. Perrell*
North Carolina State University, Raleigh, North Carolina 27695
W. D. Erickson†
NASA Langley Research Center, Hampton, Virginia 23681-0001
and
G. V. Candler‡
University of Minnesota, Minneapolis, Minnesota 55455

A computational method for calculating supersonic two-dimensional nozzle flows with nonequilibrium phase change is developed. The code uses a fully implicit, finite volume formulation with Steger–Warming flux vector splitting and Jacobi point relaxation. Source terms for finite rate condensation and evaporation are constructed from the classical theories of nucleation and droplet growth. Calculations of the NASA Langley Research Center 8-ft High Temperature Tunnel nozzle are performed and compared with previously reported quasi-one-dimensional calculations and experimental data.

Nomenclature

c_v = constant volume specific heat, J/kg K
f = function of gas composition defined in Ref. 9
h_{fg} = heat of vaporization, J/kg
h^0 = heat of formation at zero Kelvin, J/kg
i, j = computational grid cell indices
K = Boltzmann's constant
Kn = Knudsen number
m = molecular mass, kg
nc = number of droplet classes
ns = number of chemical species
Pr = Prandtl number
p = pressure, Pa
q_c, q_e = condensation, evaporation coefficients
R = specific gas constant, J/kg K
r = droplet radius, m
T = temperature, K
u = x-velocity component, m/s
v = y-velocity component, m/s
x, y = coordinate directions, m
β = empirical constant
γ = ratio of specific heats
κ = thermal conductivity of gas mixture, W/m K
μ = viscosity of gas mixture, kg/m s
ξ = constant defined in Ref. 9
ρ = density of gas mixture, kg/m^3
σ = surface tension, N/m

Subscripts
H_2O = water vapor
rot = rotational
s = chemical species
sat = saturation conditions
tr = translational
vib = vibrational
w = liquid water
$*$ = critical

Received May 15, 1995; revision received Nov. 15, 1995; accepted for publication Nov. 16, 1995.

*Graduate Student; currently Postdoctoral Research Associate, National Research Council, Washington, DC 20418; also NASA Langley Research Center, Hypersonic Airbreathing Propulsion Branch, Hampton, VA 23681-0001. Member AIAA.
†Chief Scientist, Retired, Hypersonic Vehicles Office.
‡Associate Professor, Department of Aerospace Engineering and Mechanics, 107 Akerman Hall, 110 Union Street SE. Member AIAA.

Introduction

THIS study addresses condensation in combustion-heated wind tunnels resulting from expanding the combustion products to temperatures below the saturation point. Condensation has been observed in the U.S. Air Force Arnold Engineering Development Center's Aerospace Propulsion Test Unit (APTU) and NASA Langley Research Center's 8-ft High Temperature Tunnel (8′HTT).

In a combustion-heated wind tunnel, the thermal energy of the gas is elevated by burning a fuel in the settling chamber, enabling expansion to higher Mach numbers. The APTU is fueled by isobutane, and the 8′HTT by natural gas. One product of hydrocarbon combustion is water vapor. Condensation of water vapor in combustion-heated wind tunnels, and in the 8′HTT in particular, is the focus of this study. Condensation removes mass from and adds the energy of vaporization to the gas phase. Consequently, the temperature increases, and the Mach number decreases. Drag forces on the water droplets may also be significant.

Codes that model condensation as an equilibrium process have been available for some time.[1] However, it is not safe to generalize about their sufficiency for applications to very high-speed flows. In some cases they may be adequate for engineering purposes, whereas the extreme opposite approach, a noncondensing calculation, may produce more realistic results in others. A number of theoretical studies[2–5] have addressed the thermophysics of phase change as a finite rate process. Other researchers have used results from these studies as the basis for quasi-one-dimensional calculations of nozzle flows of steam,[6–8] or of steam in a noncondensing carrier gas.[9] This study extends the work reported in Ref. 9 to develop a methodology, based upon modern computational fluid dynamics (CFD) practices, for computing hypersonic flows of condensing gases in two dimensions. It will be used to compute nonequilibrium two-phase flows in the 8′HTT nozzle and spatially characterize the flowfield at the entrance to the test section. Evidence from the 8′HTT indicates that condensation varies considerably across the test section.

Physical Modeling

The flowfield is modeled as two separated phases: 1) a continuous gas and 2) a disperse liquid. The term disperse denotes that liquid droplets do not interact with one another, or exchange conserved quantities by collision. The liquid phase is modeled as a set of droplet classes, each consisting of a certain size droplet. The conservation equations for the gas phase and each of the droplet classes are solved simultaneously. Source terms are constructed to model finite rate exchange of conserved quantities between the phases.

Gas Phase

The governing equations for the gas phase are the Navier–Stokes equations in axisymmetric coordinates:

$$\boldsymbol{U}_t + \boldsymbol{F}_x + [(y\boldsymbol{G})_y/y] = \boldsymbol{W} \tag{1}$$

The vector of conserved quantities is $\boldsymbol{U}$: the chemical species mass densities, the x- and y-momentum densities, and the total energy density:

$$\boldsymbol{U} = (\rho_1, \ldots, \rho_{ns}, \rho u, \rho v, E)^T \tag{2}$$

The total energy density is

$$E = T\sum_{s=1}^{ns} \rho_s c_{v_{\text{tr,rot}_s}} + E_{\text{vib}} + \rho\frac{u^2 + v^2}{2} + \sum_{s=1}^{ns} \rho_s h_s^0 \tag{3}$$

The vibrational energy is assumed to be in equilibrium with the translational and rotational energies because of the high rate of exchange induced by water vapor.[10]

The fluxes of conserved quantities in the x and y directions are defined in the usual way.[11–13] These are $\boldsymbol{F}$ and $\boldsymbol{G}$, respectively.

The vector of source terms is $\boldsymbol{W}$, which accounts for the interphase transfer of mass from evaporation and condensation, momentum from drag forces on the droplets, and energy from convective heat transfer and phase changes. The vector $\boldsymbol{W}$ also contains the axisymmetric source term for radial momentum.

Liquid Phase

The correct way to calculate the finite rate exchange processes between the phases is in a Lagrangian coordinate system, i.e., following the droplet pathlines z:

$$\boldsymbol{U}_z\frac{\mathrm{d}z}{\mathrm{d}t} = \boldsymbol{W} \tag{4}$$

No generalization can be made regarding the droplet pathlines, as momentum transfer between the phases is modeled as a nonequilibrium process. That is, droplet velocities are computed as functions of their sizes, in contrast to previous studies that assumed that droplets move at the same speed as the gas. This necessitates modeling the distribution of droplet sizes discretely, since there is no known way to construct an infinite number of Lagrangian coordinate systems, as a continuous distribution of droplet sizes would require. The distributions of temperature and velocity for each discrete size class are assumed to be narrow enough to allow their representation by a single temperature and velocity at each point in the flowfield.

With even a small number of droplet classes, constructing pathlines and integrating Eq. (4) along each is difficult, if not intractable, since pathlines can begin at any point, and droplets move among the classes as they travel. It is permissible to simplify the kinematics with an Eulerian approximation to the left-hand side of Eq. (4), so long as the Lagrangian description is maintained in constructing the source terms. The total derivative is set equal to a local time derivative plus a spatial flux derivative, which is resolved into components, giving a governing equation set that is identical in form to that for the gas phase:

$$\boldsymbol{U}_{k_t} + \boldsymbol{F}_{k_x} + [(y\boldsymbol{G}_k)_y/y] = \boldsymbol{W}_k \tag{5}$$

The vectors are subscripted k to denote a specific class. The vector of conserved variables for the liquid phase is

$$\boldsymbol{U}_k = \rho_w n_k V_k(1, u_k, v_k, c_{v_w}T_k + e_w^0)^T \tag{6}$$

where ρ_w is the density of liquid water, and n_k and V_k are the number density and volume per droplet, respectively, of class k droplets. The internal energy of liquid water at zero Kelvin is e_w^0.

The liquid fluxes are just the vector of conserved variables times the appropriate velocity component:

$$\boldsymbol{F}_k = u_k\boldsymbol{U}_k \qquad \boldsymbol{G}_k = v_k\boldsymbol{U}_k \tag{7}$$

The liquid kinetic energy is not included as a conserved variable. Doing so essentially gives five equations for four unknowns, if one considers that liquid kinetic and thermal energy conservation can be expressed as two equations, since the two forms of energy cannot be directly converted in a disperse phase, as they can in the gas phase, by molecular collisions. That is, kinetic energy conservation overspecifies the system of equations, since the mass and velocity components are known from the first three equations. Experience has shown that conserving liquid kinetic energy produces erroneous temperatures.[12]

Source Terms

The finite rate processes that transfer conserved quantities between the phases and between the droplet classes are the source terms. The gas phase sources are equal and opposite those for the liquid phase, enforcing conservation. The one exception is that gas phase sources include kinetic energy terms, whereas liquid phase sources do not, as explained earlier.

Nucleation

The onset of condensation is modeled according to the classical nucleation theory,[5] which assumes spontaneous formation from the subcooled vapor of droplets containing about 100 molecules. The rate of nucleation is

$$J = \frac{q_c}{1 + Q}\sqrt{\frac{2\sigma}{\pi m_{\text{H}_2\text{O}}^3}}\frac{\rho_{\text{H}_2\text{O}}^2}{\rho_w}\exp\left(\frac{-4\pi r_*^2\sigma}{3KT}\right) \tag{8}$$

where

$$Q = \frac{2(\gamma_{\text{H}_2\text{O}} - 1)}{(\gamma_{\text{H}_2\text{O}} + 1)}\frac{h_{fg}}{R_{\text{H}_2\text{O}}T}\left(\frac{h_{fg}}{R_{\text{H}_2\text{O}}T} - \frac{1}{2}\right) \tag{9}$$

is Kantrowitz's[4] correction factor for nonisothermal nucleation. Nuclei are formed at the critical radius, the radius of a droplet in metastable equilibrium with the gas phase:

$$r_* = 2\sigma/[\rho_w R_{\text{H}_2\text{O}}T\,\ell n(P_{\text{H}_2\text{O}}/P_{\text{sat}})] \tag{10}$$

Drag

The rate of momentum transfer is the drag force:

$$\boldsymbol{D}_k = n_k\frac{1}{2}C_D\rho\begin{bmatrix}(u - u_k)|u - u_k| \\ (v - v_k)|v - v_k|\end{bmatrix} \tag{11}$$

The drag coefficient is a function of the Mach and Reynolds numbers based upon the vectorial relative velocity, as derived by Carlson and Hoglund[14]:

$$C_D = \frac{24}{Re}\frac{(1 + 0.15Re^{0.687})\{1 + \exp[-(0.427/M^{4.63}) - (3/Re^{0.88})]\}}{1 + (M/Re)\{3.82 + 1.28\exp[-1.25(Re/M)]\}} \tag{12}$$

The drag force on the droplets also transfers kinetic energy from the gas phase:

$$W_{KE} = -\sum_{k=1}^{nc} D_{x_k} u_k + D_{y_k} v_k + \frac{(D_{x_k}^2 + D_{y_k}^2)}{2U_{k_1}} \Delta t \qquad (13)$$

The last term in the summation accounts for the variation of the droplet velocity over the time step Δt, assuming constant drag.[12]

Droplet Growth

Droplet growth from condensation and evaporation is modeled by simultaneously integrating two equations for mass and energy transfer. These are, respectively,

$$\frac{dr}{dt} = \frac{2q_c}{\rho_w(2 - q_c)} \left(\frac{P_{H_2O}}{\sqrt{2\pi R_{H_2O} T}} - \frac{q_e}{q_c} \frac{P_s}{\sqrt{2\pi R_{H_2O} T_k}} \right) \qquad (14)$$

$$\frac{r}{3} \rho_w c_{v_w} \frac{dT_k}{dt} = h_{fg} \rho_w \frac{dr}{dt} - \frac{(\kappa/r)(T_k - T)}{[1/(1 + 2\beta Kn)] + (\xi/f)(Kn/Pr)} \qquad (15)$$

Equation (14) is simply the difference in molecular flux to the surface from the gas, and re-evaporative flux from within the droplet. Equation (15) expresses the rate of change of droplet temperature as a function of the rate of latent heat release from condensation, and convection to the gas. From these equations, Young[8] has derived a single analytically integrable growth rate equation by approximating the droplet temperature as a function of the gas properties and droplet size. The details are given in Refs. 8, 9, and 12.

Young's procedure assumes that the gas is subcooled. It has been used successfully in quasi-one-dimensional nozzle calculations.[8,9] In a two-dimensional calculation, droplets can be captured in superheated regions caused by boundary-layer growth, and compression caused from wall effects. In these regions Eqs. (14) and (15) must be simultaneously integrated numerically.

Solution Procedure

The source vector for nucleation is easily constructed from Eq. (8). Droplets are formed at the velocity and temperature of the gas:

$$W_{nuc_k} = \rho_w V_k J(1, u, v, c_{v_w} T + e_w^0)^T \qquad (16)$$

The class k into which droplets nucleate is chosen such that $r_{k-1} < r_* < r_k$. This criterion is established because droplets smaller than the critical size evaporate rapidly. Hence, placing nuclei in a class for which $r < r_*$ has no net effect.

The components of the drag force [Eq. (11)] comprise elements 2 and 3 of the momentum source vector for class k.

The drop growth equations, unlike the other rate equations, cannot be integrated locally. To do so would result in unbounded growth. Equations (14) and (15) must be integrated along the droplet path. Since we have approximated the kinematics with an Eulerian description, this is accomplished by integrating the growth equations for each class over a cell residence time, and using the results to reassign class designations as droplets cross cell boundaries. For example, if in one cell residence time, class k droplets grow to a radius $\hat{r}$ that falls between the radii for adjacent classes l_1 and l_2, they are reapportioned between classes l_1 and l_2 such that the mass transferred between phases equals that for growth to $\hat{r}$. The fractions of class k droplets reassigned to classes l_1 and l_2 are

$$\psi_{l_1} = [(r_{l_2}^3 - \hat{r}^3)/(r_{l_2}^3 - r_{l_1}^3)] \qquad \psi_{l_2} = 1 - \psi_{l_1} \qquad (17)$$

Droplet growth then can be thought of as a source of flux. The liquid fluxes are now written as a difference of effluxes from the cell, and influxes into the cell. The effluxes are defined as the fluxes were previously [Eq. (7)]. The influxes are constructed taking account of the growth in adjacent cells. Equation (5) becomes

$$U_{k_t} + (F - \Phi)_{k_x} + \{[y(G - \Gamma)_k]_y / y\} = W_k \qquad (18)$$

where $\Phi_k = \tilde{u}_k \tilde{U}_k$, and $\Gamma_k = \tilde{v}_k \tilde{U}_k$. The virtual vector of conserved quantities resulting from droplets of another class growing to the size of class k droplets is $\tilde{U}_k$. Class k condensing and evaporating give, respectively,

$$\tilde{U}_l = \psi_l \begin{bmatrix} \frac{V_l}{V_k} U_{k_1} \\ U_{k_2} + U_{k_1} \left(\frac{V_l}{V_k} - 1 \right) u \\ U_{k_3} + U_{k_1} \left(\frac{V_l}{V_k} - 1 \right) v \\ \frac{V_l}{V_k} U_{k_1} (e_w^0 + c_{v_w} \tilde{T}_l) \end{bmatrix} \qquad (k < l) \qquad (19)$$

$$\tilde{U}_l = \psi_l \frac{V_l}{V_k} \begin{bmatrix} U_{k_1} \\ U_{k_2} \\ U_{k_3} \\ U_{k_1} (e_w^0 + c_{v_w} \tilde{T}_l) \end{bmatrix} \qquad (k > l) \qquad (20)$$

$\tilde{T}_l$ is the temperature that results from integrating the growth equations (either numerically or by Young's method) to r_l.

The gas phase source vector for droplet growth is the divergence of the efflux minus the influx. This enforces conservation, as a comparison of the following equation with Eq. (18) illustrates:

$$W_{growth} = \sum_{k=1}^{nc} \left(\left[F_k - \sum_{l=l_1}^{l_2} \Phi_l \right]_x + \left\{ \left[y \left(G_k - \sum_{l=l_1}^{l_2} \Gamma_l \right) \right]_y \Big/ y \right\} \right) \qquad (21)$$

Equations (1) and (18) are discretized in general coordinates, and solved simultaneously as a single vector equation of dimension $ns + 3 + 4nc$. A finite volume, fully implicit formulation is used. The result is a block pentadiagonal matrix equation of dimension $i_{max} \times j_{max}$. Each block has dimension $ns + 3 + 4nc$, the number of conserved variables. The matrix equation is solved by point Jacobi iteration.

The inviscid fluxes are evaluated using Steger–Warming[13] flux vector splitting; the viscous fluxes by central differencing the fluid property derivatives. The liquid fluxes are evaluated in terms of the variables in the upstream cell.[15]

Calculations

Two cases were computed using the geometry of the NASA LaRC 8'HTT: a cylindrical throat, 7.14 cm in radius and 2.85 cm in length; a conical expansion section from $x = 2.85$ cm to 5.47 m; a contoured section from $x = 5.47$ m to the tunnel exit at 15.71 m. The expansion ratio is 523.4. The computational mesh for the complete nozzle contained 197 cells in the axial direction, and 89 cells in the radial direction. For each case the procedure was to first perform a noncondensing calculation on the entire nozzle. The throat (inflow boundary) conditions were computed assuming an isentropic expansion with fixed composition from given stagnation conditions. To minimize storage and CPU requirements, the condensing calculations were then performed only on the downstream end of the tunnel. The inflow boundary for the condensing calculation was located just upstream of the saturation line. The location of the saturation line was determined from the noncondensing calculation. The noncondensing calculation also provided the

inflow boundary conditions and the initial conditions for the condensing calculation, as well as a basis for discussing the effects of condensation. An adiabatic wall boundary condition was used in all calculations.

Case 1

Case 1 was used for the initial code development. The stagnation conditions for case 1 were the same as those for case 5 of Ref. 13, allowing a qualitative comparison between the previous quasi-one-dimensional calculation, and the present two-dimensional calculation. The total temperature and pressure were 1900 K and 25 MPa, respectively. The mole fractions of water vapor, oxygen, nitrogen, and carbon dioxide were 0.156, 0.21, 0.556, and 0.078, respectively. For the throat conditions this gave 1684.5 K, 13.831 MPa, and 828.62 m/s.

The grid size for the condensing calculation was 60 × 89. Four classes of droplets were used, with diameters spanning three orders of magnitude: $d_1 = 1.5 \times 10^{-9}$ m, $d_2 = 10^{-8}$ m, $d_3 = 10^{-7}$ m, and $d_4 = 10^{-6}$ m. The size of the largest class was chosen to be slightly greater than the largest droplet size computed in Ref. 9. The size of the smallest class was chosen to match the size of the nuclei in the zone of highest nucleation rate, as closely as possible. The critical diameter is in the range of 1–1.5 nm in this region.

Figure 1 illustrates the nucleation zone. The contours are closely spaced, indicating a rapid rise in the nucleation rate. In fact, no sensible nucleation occurs before $x \approx 7$ m, even though the vapor becomes saturated 1 m upstream. The maximum value of about 10^{20} nuclei/m^3/s occurs on the centerline at $x \approx 8$ m.

Growth of existing droplets removes more mass from the gas phase than nucleation does, as Fig. 2 illustrates. At the downstream end of the nucleation zone the flowfield contains less than 1% liquid water. This value rises to nearly 3% on the centerline at the nozzle exit plane. Note the variation of the liquid content in the radial direction at the exit plane.

Figure 3 compares the droplet and gas temperatures along the nozzle centerline. The solid symbols marking the endpoints of the temperature curves for each class indicate positions where the particular classes appear or disappear. Class 1, into which droplets nucleate, first appears at the same temperature as the gas. The larger classes first appear at higher temperatures, since condensation releases the latent heat of vaporization to them. At $x \approx 8.5$ m the temperature of class 1 increases as well. At this point, presumably condensation has a greater effect than nucleation on the average temperature of class 1 droplets.

Figure 3 also shows the gas temperature beginning to increase shortly after the onset of condensation, even though the gas is expanding. This is caused by convective heat transfer from the water droplets. The smaller classes evaporate immediately after the gas temperature rises above their temperatures. Class 1 is repopulated by evaporating class 2 droplets in one grid cell at $x \approx 12.5$ m. Evaporation of the larger classes repopulates classes 1 and 2 near the exit. Classes 1 and 2 are at lower temperatures because of the loss of latent heat by classes 3 and 4 upon evaporation.

Figures 4–7 compare the flowfields calculated without, and with condensation. Figure 4 shows the degree of subcooling as the difference between the saturation temperature for the

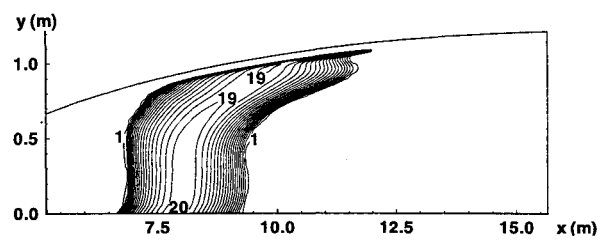

Fig. 1 Case 1: log nucleation rate (m^{-3}s^{-1}).

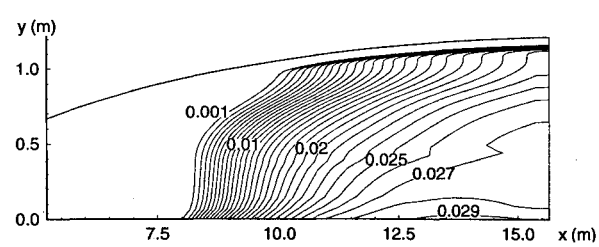

Fig. 2 Case 1: mass fraction of liquid.

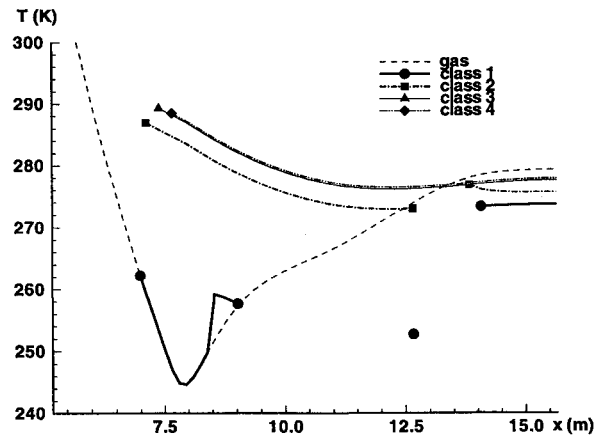

Fig. 3 Case 1: nozzle centerline temperatures (K).

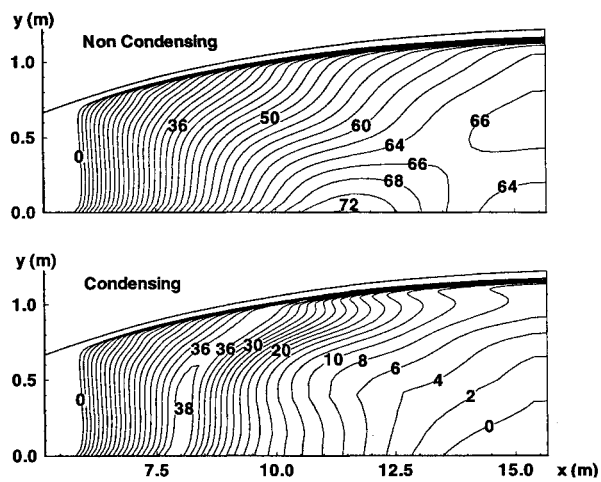

Fig. 4 case 1: subcooling (K).

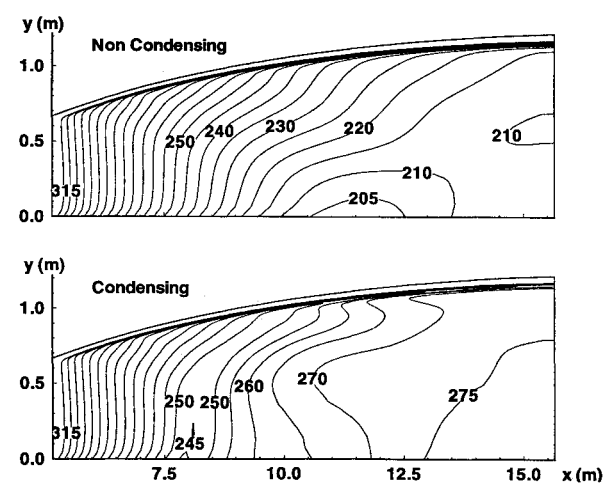

Fig. 5 Case 1: gas temperature (K).

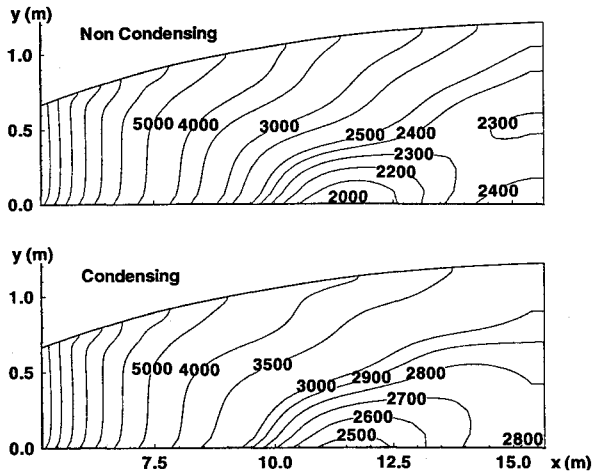

Fig. 6 Case 1: pressure (Pa).

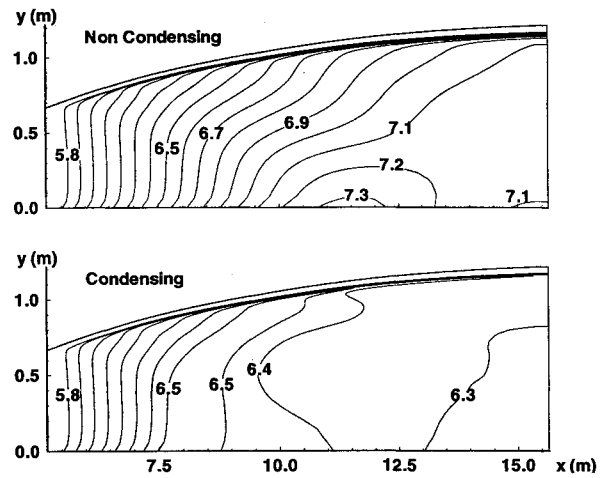

Fig. 7 Case 1: Mach number.

partial pressure of water vapor and the gas temperature. The flowfields are substantially the same upstream of the 36 K subcooling line. The nucleation rate peaks slightly beyond this line.

Most important, regarding the goal of characterizing the test section flowfield, are the next three figures. They show temperature and pressure increases of around 60 K and 450 Pa, respectively, and a decrease of about 0.8 (11%) in Mach number at the nozzle exit plane.

The exit plane velocity is only 5 m/s lower in the condensing calculation than in the noncondensing calculation. The gas velocity increases by only about 30 m/s between the point where condensation begins and the tunnel exit. The droplet and gas velocities differ by less than 2 m/s throughout the flowfield.

Figures 8 and 9 are plots of the subcooling, nucleation rate, and liquid mass fraction along the centerline, as calculated here and in Ref. 9. The maximum subcooling is about 40 K in both cases. The peak nucleation rate calculated here is slightly greater, as is the maximum mass fraction of water. One notable difference is the location of condensation onset, about 7.5 m here, vs 8.5 m. This could be because of the two dimensionality, or the lack of chemical reaction modeling in the present work. Reference 9 employed equilibrium chemistry calculations. Reference 9 also showed the subcooling collapsing more rapidly than the present work does. This is a result of the small number of droplet classes, as will be shown.

Another difference is that here the gas not only returns to equilibrium, but actually becomes superheated. This is the result of a region of recompression beginning at about 11.5 m. This recompression is evident in Fig. 6 for both the condensing and noncondensing calculations.

This effect could not be produced in a one-dimensional calculation. Overexpansions and subsequent recompressions resulting from imperfect nozzle contour design are apparent only in two- (or three-) dimensional calculations.

Finally, it is noteworthy that the gas and liquid properties vary smoothly across the saturation line, both in the recompression region, and at the edge of the boundary layer. Recall that Young's analytical integration of the droplet growth equations assumes that the gas is subcooled. Therefore it was necessary to integrate them numerically in and around superheated regions. The smooth blending of the solutions from the two techniques ostensibly attests to the validity of Young's method.

Case 2

The stagnation conditions for case 2 were measured during actual tests conducted recently in the 8'HTT. The total tem-

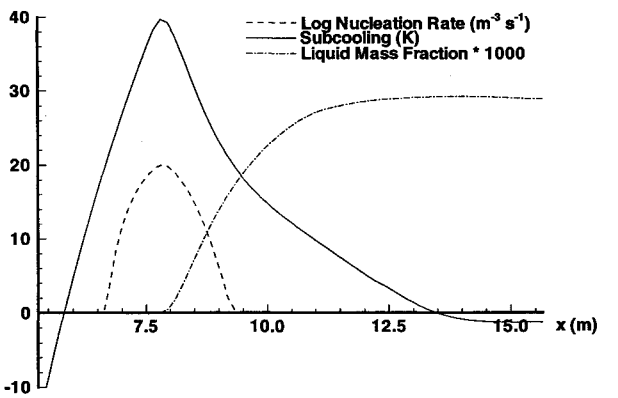

Fig. 8 Case 1: nozzle centerline conditions.

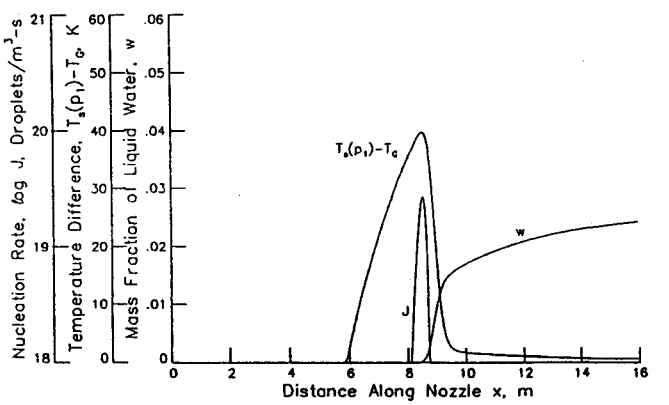

Fig. 9 One-dimensional nozzle conditions (from Ref. 9).

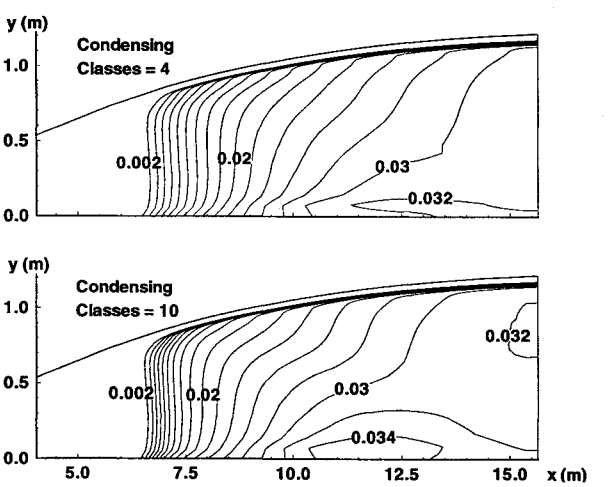

Fig. 10 Case 2: mass fraction of liquid.

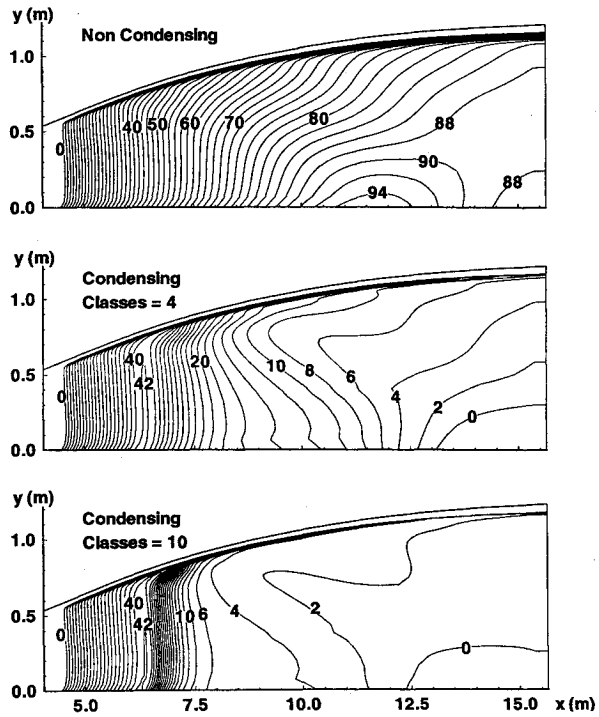

Fig. 11 Case 2: subcooling (K).

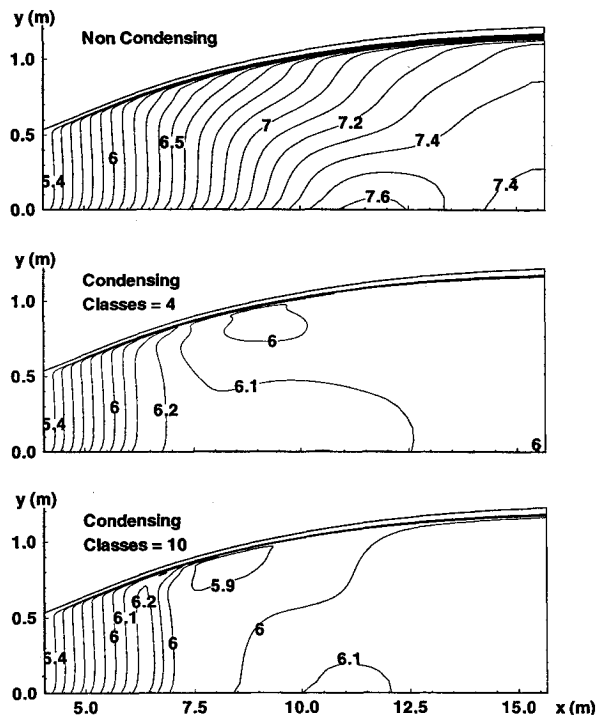

Fig. 12 Case 2: Mach number.

perature and pressure were 1667 K and 13.8 MPa. Mole fractions of water vapor, oxygen, nitrogen, and carbon dioxide were 0.12, 0.21, 0.61, and 0.06, respectively. The throat conditions were 1464.4 K, 7.5818 MPa, and 737.93 m/s. The grid size for case 2 was 73 × 89.

This case included a refinement study, to determine the effect, if any, of increasing the number of droplet classes. The first of two condensing flow calculations was performed using the same four droplet class definitions as case 1. The calculation was then restarted from the first solution with 10 droplet classes. The diameter of the first class was defined as 1 nm. For $k = 2-10$, $d_k = \sqrt[3]{10}d_{k-1}$. This yielded a largest class size of 1 μm, as before.

The results show only slightly more condensation occurring in the 10-class case, but it occurs further upstream. Figure 10 shows tighter clustering of the contours of constant liquid mass fraction w, up to $w \approx 0.02$. Contour lines beyond $w \approx 0.02$ are shifted upstream by about 1 m.

Figures 11–13 compare various flowfield parameters between the condensing and noncondensing calculations. The effects of condensation, that is, the Mach number decrease and temperature increase, have also shifted upstream a bit with the finer discretization of droplet sizes.

Figure 14 compares static pressures on the wall, calculated with and without condensation, and measurements from the 8'HTT. The accuracy of the measurements is within plus or minus one-quarter of 1%. The condensing calculations match the data much better than the noncondensing calculations do. The increased upstream condensation with 10 classes is evident in this figure also.

Code Performance

Calculations were done on a Cray Y-MP. The two-phase code's memory and CPU requirements are significantly greater than those of the equivalent single-phase code because of the large number of conserved variables introduced via the droplet size discretization. Case 1 was calculated in 25 CPU hours; case 2 (4 class) in 36 CPU hours. The case 2 10-class calculation, which was started from the solution of the 4-class calculation, required an additional 24 h. The memory require-

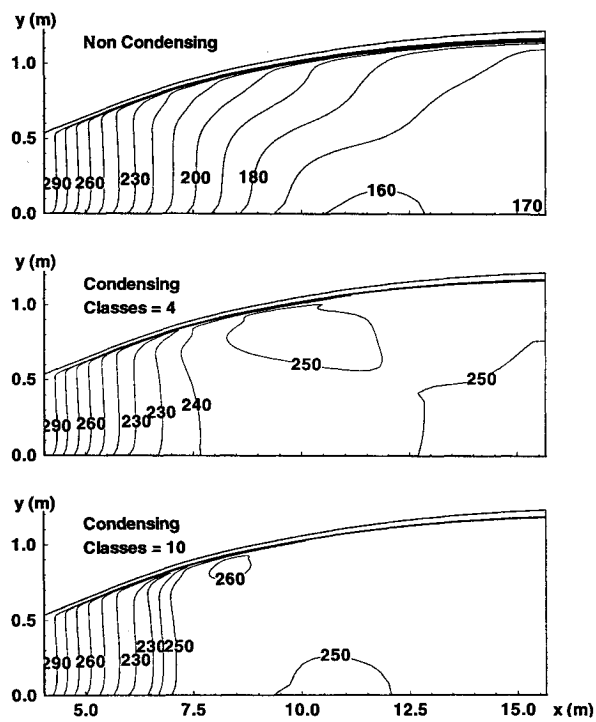

Fig. 13 Case 2: gas temperature (K).

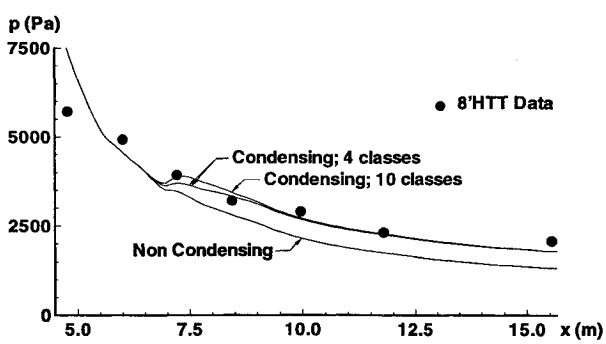

Fig. 14 Case 2: wall pressure (Pa).

ments for the three calculations were 14, 18, and 41 MW, respectively.

Conclusions

An axisymmetric code for condensing nozzle flows has been developed and tested. The code utilizes the classical theories of droplet nucleation and finite rate growth. Results of calculations are at least qualitatively correct, as regards the effect of condensation on the gasdynamics. Calculations of condensing flows show an increase in temperature and pressure, and a decrease in Mach number, compared to noncondensing calculations. Computed wall pressures for the condensing cases agree well with experimental data.

The accuracy of the solution improves with increasing numbers of droplet classes. A fair approximation is obtainable with only four classes representing a distribution of diameters spanning three orders of magnitude. Ten classes produce a noticeable difference in the flowfield immediately after the onset of condensation. The subcooling collapses back towards equilibrium much more quickly with 10 classes, than with four. The differences in the flowfield downstream, near the tunnel exit, are less pronounced. For most practical purposes, 10 classes are probably sufficient.

The method developed herein is quite computationally intensive because of the size of the matrix equation resulting from the discretization of the liquid phase into droplet classes. With each additional class, the dimension of each block in the matrix increases by four, the number of conserved variables per class. However, the momentum components comprise two of the four conserved variables, to permit interphase momentum transfer to be calculated as a nonequilibrium process as well. In retrospect, this was unnecessary in the code's present application, since the calculations show that the droplets move very nearly at the same speed as the gas.

Recommendations

With regard to the overall efficiency of the present nozzle code, the following improvements are recommended. First, the droplet velocities should be set equal to the gas velocities. This assumption will permit removing the source terms and Jacobians for momentum transfer, and also reduce the number of conserved variables for each class by two. (In other applications, where higher gas velocity gradients are expected, it may be essential to retain these terms.)

Secondly, grid solution-adaption should be employed. In regions where the two-phase dynamics are potentially active, the axial gridlines should be adapted to coincide with the streamlines. This will eliminate liquid fluxes and Jacobians in the radial direction, reducing the work of the matrix solution routines by more than half. In effect, these modifications will reduce work of the matrix solution routines by more than half. In effect, these modifications will reduce the liquid phase dynamics to a set of quasi-one-dimensional equations, the one dimension being the droplet pathline. This approach is, in fact, a more physically correct way to model the kinematics of a disperse phase.

Some comments on the limitations of the classical nucleation and drop growth theories are in order here. The agreement of calculation with static pressure measurements, and with our intuition regarding temperature and Mach number trends, are presented as justification for use of the classical theories. Nevertheless, historically there has been a paucity of experimental data characterizing the liquid phase in nonequilibrium condensing flows. Those measurements that have been made do not generally substantiate nucleation rate calculations. It has been suggested that because the nucleation and growth rates vary so strongly with subcooling, they are self-correcting to some degree. Overpredicting condensation at one point leads to underprediction at a point slightly downstream; overprediction of the nucleation rate causes underprediction of the growth rate. Thus, they are sufficient for engineering applications to large-scale flows. Accurate characterization of the liquid phase merits attention in CFD applications to smaller-scale flows, external flows, rapid expansions, flows over turbine blades, or two-phase combustion, for example.

Acknowledgments

This work was supported by Contract NAG-1-1470 with the NASA Langley Research Center, and by NASA Grant NAGW-1331 to the Mars Mission Research Center at North Carolina State University. Computer support was provided by the North Carolina Supercomputing Center, Research Triangle Park, North Carolina; by NASA Langley Research Center, Hampton, Virginia; and by the University of Minnesota, Minneapolis, Minnesota.

References

[1]Gordon, S., and McBride, B. J., "Computer Program for Calculation of Complex Chemical Equilibrium Compositions, Rocket Performance, Incident and Reflected Shocks, and Chapman-Jouget Detonations," NASA SP-273, Jan. 1957.

[2]Frenkel, J., *Kinetic Theory of Liquids*, Dover, New York, 1946.

[3]Gyarmathy, G., "Zur Wachstumsgeschwindigkeit kleiner Flüssigkeitstropfen in einer übersättigten Atmosphäre," *Zeitschrift für Angewandte Mathematik und Physik*, Vol. 14, No. 3, 1963, pp. 280–293.

[4]Kantrowitz, A., "Nucleation in Very Rapid Vapor Expansions," *Journal of Chemical Physics*, Vol. 19, No. 9, 1951, pp. 1097–1100.

[5]Volmer, M., and Weber, A., *Z. Physik. Chem.* (Leipzig), Vol. 119, 1926, pp. 277–301.

[6]Gyarmathy, G., "Condensation in Flowing Steam," *Two-Phase Steam Flow in Turbines and Separators*, edited by M. J. Moore and C. H. Sieverding, Hemisphere, Washington, DC, 1976, pp. 127–189.

[7]Hill, P. G., "Condensation of Water Vapor During Supersonic Expansion in Nozzles," *Journal of Fluid Mechanics*, Vol. 25, Pt. 3, 1966, pp. 593–620.

[8]Young, J. G., "The Spontaneous Condensation of Steam in Supersonic Nozzles," *Physico-Chemical Hydrodynamics*, Vol. 3, No. 1, 1982, pp. 57–82.

[9]Erickson, W. D., Mall, G. H., and Prabhu, R. K., "Finite-Rate Water Condensation in Combustion-Heated Wind Tunnels," NASA TP-2833, Sept. 1988.

[10]Chernyavina, N. M., "Vibrational Relaxation and Radiation of Water Vapor Behind a Shock Wave," *Fluid Mechanics—Soviet Research*, Vol. 13, No. 3, 1984, pp. 100–106.

[11]Candler, G. V., "The Computation of Weakly Ionized Hypersonic Flow in Thermochemical Nonequilibrium," Ph.D. Dissertation, Stanford Univ., Stanford, CA, June 1988.

[12]Perrell, E. R., "Computation of Combustion Heated Hypersonic Wind Tunnel Flows in Phase Nonequilibrium," Ph.D. Dissertation, North Carolina State Univ., Raleigh, NC, July 1994.

[13]Steger, J., and Warming, R. F., "Flux Vector Splitting of the Inviscid Gasdynamic Equations with Application to Finite Difference Methods," NASA TM-78605, 1979.

[14]Carlson, D. J., and Hoglund, R. F., "Particle Drag and Heat Transfer in Rocket Nozzles," *AIAA Journal*, Vol. 2, No. 11, 1964, pp. 1980–1984.

[15]Candler, G. V., Levin, D. A., Collins, R. J., Erdman, P. W., Zipf, E., and Howlett, C., "Comparison of Theory with Plume Radiance Measurements from the Bow Shock Ultraviolet 2 Rocket Flight," *Journal of Thermophysics and Heat Transfer*, Vol. 7, No. 4, 1993, pp. 709–716.